

Biodegradable Mesoporous Manganese Carbonate Nanocomposites for LED Light-Driven Cancer Therapy *via* Enhancing Photodynamic Therapy and Attenuating Survivin Expression

Lihua Li (✉ lihua361@126.com)

South China University of Technology <https://orcid.org/0000-0001-6651-2146>

Lingling Chen

Southern Medical University

Ling Huang

South China University of Technology

Xiangling Ye

Guangzhou University of Chinese Medicine

Zefeng Lin

South China University of Technology

Xiaoming Wei

South China University of Technology

Xianfeng Yang

South China University of Technology

Zhongmin Yang

South China University of Technology

Research Article

Keywords: Triple negative breast cancer, mesoporous MnCO₃ nanocubes, LED light responsive, O₂ and CO₂ release, reactive oxygen species

Posted Date: September 1st, 2021

DOI: <https://doi.org/10.21203/rs.3.rs-847366/v1>

License:  This work is licensed under a Creative Commons Attribution 4.0 International License.

[Read Full License](#)

Abstract

Triple-negative breast cancer (TNBC) is one of the most daunting diseases, and low toxicity and efficient approaches are in urgent demand. Herein, we developed degradable mesoporous manganese carbonate nanocubes (MnCO_3 NCs), incorporated with survivin shRNA-expressing plasmid DNA (iSur-pDNA) and riboflavin (Rf), namely MRp NCs, for synergistic TNBC therapy. The MnCO_3 , itself, could generate O_2 and CO_2 under H_2O_2 and thus improve the hypoxia and acidic tumor microenvironment (TME). Furthermore, the MnCO_3 NCs exhibited high Rf loading capacity and iSur-pDNA delivery ability after polyethyleneimine modification. Specifically, MRp NCs decompose in TME, meanwhile they deprived the endogenous expression of survivin gene and significantly amplified the generation of reactive oxygen species after exposure to LED light, resulting in serious tumor destruction. The multifunctional MRp NCs with LED light-driven characters are able to provide a high efficiency, low toxicity and promising strategy for TNBC therapy.

1. Introduction

Triple-negative breast cancer (TNBC) is an important and intractable subtype of breast cancer due to lack of biomarkers and its high metastasis¹. There was no significant progress in TNBC treatment during the past decades². Traditional chemotherapies are still the main approaches for TNBC therapy, but they exhibit high toxicity and low efficiency, resulting in poor life quality and low survival rates. It is urgent to develop new approaches with high safety, low toxicity, and high efficiency to deal with TNBC³.

Photodynamic therapy (PDT) and chemodynamic therapy (CDT) based on reactive oxygen species (ROS) provide new alternative opportunities for cancer therapy. They exhibit high selectivity in cancer therapy and could be activated by inner (e.g., low pH, abundant glutathione, and H_2O_2)⁴⁻⁵ or external stimulus (light, magnetic field, and heat)⁶⁻⁸ compared with chemotherapy. Manganese-based nanoparticles have been widely reported for cancer theranostic because of their excellent tumor microenvironment (TME) responsive characters and potential CDT effect⁹. These features selectively damage the tumor cells while protecting the normal cells because they are restrained in the specific tumor regions. We previously found Bi@MnO_x nanoparticles could respond to both inner and external stimuli, exhibiting a mutual reinforcement for cancer therapy¹⁰. Recently, researchers have focused on the catalytic reaction of MnO_x ¹¹, and various ROS-based nanozymes have been developed for cancer therapy (e.g., MnO_x -SPNs¹², Au-MnO ¹³, and MnO_x ¹⁴). However, it is still difficult to tackle with TNBC only using CDT/PDT approaches.

To address these issues, we developed MnCO_3 /Rf/pDNA nanocomposites (denoted as MRp NCs) which consisted of mesoporous MnCO_3 nanocubes (NCs) loading with riboflavin (Rf) and survivin shRNA expressing plasmid (iSur-pDNA) for combined TNBC therapy. Rf, as a necessary nutrient for the human body, could also work as a photosensitizer. Its ROS production was significantly amplified in the presence of MnCO_3 NCs. Moreover, the polyethyleneimine (PEI) modified MnCO_3 NCs could efficiently deliver iSur-pDNA to 4T1 cells for survivin gene silencing. The MRp NCs illustrate multiple roles in TNBC therapy: (i)

as TME ameliorative agents for improving tumor acidity and hypoxia; (ii) as a biodegradable drug and pDNA carrier; The high surface potential enables the PEI-MnCO₃ NCs with high pDNA transfection efficiency; (iii) as an assistant for combined TNBC therapy. The MRp NCs can be decomposed under simulated TME solution, resulting in the release of Mn²⁺, O₂ and CO₂ for enhancing PDT and CDT, moreover, the generated O₂ and CO₂ could also destroy the tumor tissue, and the delivered pDNA could deprive the survivin gene, thus enhancing tumor cell destruction (Scheme 1).

2. Experiment Section

2.1 Materials. Cetyltrimethylammonium bromide (CTAB), MnCl₂·4H₂O, 1-butanol, cyclohexane, KHCO₃, NH₄HCO₃, polyethyleneimine (PEI, 10,000 KDa), and ethanol were purchased from Aladdin Co., 1,3-diphenylisobenzofuran (DPBF), Ltd (Shanghai, China). Riboflavin, 30% hydrogen peroxide (H₂O₂), Calcein-AM, propidium iodide (PI), and cell counting Kit-8 (CCK-8) were purchased from Sigma-Aldrich (USA) Phosphate buffer saline (PBS), fetal bovine serum (FBS), penicillin/streptomycin (PS) and Dulbecco's modified Eagle's medium (DMEM) were purchased from Gibco Life Technology (AG, Switzerland). 4% Paraformaldehyde fix solution and GSH/GSSG assay kit were obtained from Beyotime. Hypoxia detection kit was bought from Enzo Biochem. Inc. (USA). L-buthionine sulfoximine (L-BSO) was obtained from Meilun Biotechnology Co., Ltd (Dalian, China). All of chemical reagents were used as received without further purification. The *Escherichia coli* containing iSurvivin-pDNA and pGL-control was purchased from GenePharma Co., Ltd. (Shanghai, China). The iSur-pDNA and pGL-control vector were amplified in *Escherichia coli* and isolated with an EndoFree Plasmid Mega Kit (Tiangen Biotech Co., Ltd., Beijing, China) The forward primer and reverse primer sequences of survivin were: Sur-sense: 5'-AATCATGAATCCATGGCAGCCAG-3' and the reverse primer 5'-AAGAATTCATGGGTGCCCCGA-3'¹⁵. β-actin sense: 5'-CCA ACC GCG AGA AGA TGA-3' and the reverse primer 5'-CCA GAG GCG TAC AGG GAT AG-3', respectively.

2.2 Preparation of MnCO₃ NCs. The MnCO₃ synthetic process was according our previous work¹⁶. CTAB (2 g), MnCl₂·4H₂O (10 mmol) were mixed in 2.0 mL water, 3.0 mL 1-butanol and 60 mL cyclohexane, and then the mixture were vigorously stirred at room temperature, named as A solution. CTAB (8g), of KHCO₃ (19 mmol), NH₄HCO₃ (1 mmol), 8.0 mL water, 3.0 mL 1-butanol and 240 mL cyclohexane were mixed and vigorously stirred in container B. After magnetic stirring for 1 h, solution A was added to container B under continuous stirring. After reacted for another 0.5 h, the solution was centrifuged at 8,000 rpm for 10 min to remove the supernatant. The final MnCO₃ was washed with ethanol and dd H₂O for three times, and then the precipitates were extracted several times using methanol with 1% NaCl to remove the redundant CTAB.

2.3 Modification of MnCO₃ NCs. Surface modification of MnCO₃ NCs with amine-containing PEI was followed below, 0.1 g MnCO₃ NCs were dispersed in 100 mL ddH₂O with vigorously stirring, then 0.1 g PEI was added to the solution. The mixture was stirred at room temperature for another 2 h. The PEI-MnCO₃

NCs were collected by centrifugation (10,000 rpm, 10 min) and washed with water for 3 times to remove the redundant PEI.

2.4 Characterization. The powder X-ray diffraction (XRD) patterns were collected with a Siemens Kristalloflex 810 D-500X-ray diffractometer using Cu K α irradiation ($\lambda = 1.5406 \text{ \AA}$). High-resolution transmission electron microscopy was taken on a field emission scanning electron microscope (JEOL JEM-2100F, Japan). Zeta potential and hydrophilic size were measured using a zetasizer (Zetasizer Nano ZS, Malvern, UK). UV-vis-NIR absorption spectra and absorbance were examined using multifunctional microplate reader (TECAN, infinite M200 PRO, Swiss)

2.5 Drug loading. PEI-MnCO₃ NCs (500 μg) were suspended in 5 mL PBS solution, and then Rf was dispersed in the solution at a concentration of 100 $\mu\text{g mL}^{-1}$. After stirring at 4 °C for 24 h, the solution was centrifuged. And the supernatant and precipitates were collected respectively. PEI-MnCO₃/Rf NCs was named as MR. The drug loading efficiency was calculated as below:

$$\text{Drug loading efficiency (\%)} = \frac{\text{TotalRfamount} - \text{SupernatantRfamount}}{\text{TotalRfamount}} \times 100 \quad (1)$$

2.6 Extracellular O₂ Measurement. The O₂ production from PEI-MnCO₃ NCs in H₂O₂ solution was monitored by a portable dissolve oxygen meter. Briefly, different concentrations of PEI-MnCO₃ NCs (0, 100, 200 $\mu\text{g mL}^{-1}$) was added to 10 mM H₂O₂ PBS solution. The data was recorded every 5 s for 10 min using the portable dissolve oxygen meter.

ROS detection. ROS generation was detected by ESR. Typically, Rf, PEI-MnCO₃ and MRf NCs (100 μL , 0.5 mg mL⁻¹) were mixed with H₂O₂ (100 μL , 16 mM) containing the trapping agent 5, 5-dimethyl-1-pyrroline-N-oxide (DMPO, 10 μL , 10 mM). Then, the X-band ESR spectra were acquired by Bruker ELEXSYS-II spectrometer at 37 °C. The raw MnCO₃ and H₂O₂ were set as control.

2.7 Extracellular ROS Detection. 1 mM fluorescent dye 2',7'-dichlorodihydrofluorescein diacetate (DCFH-DA, Sigma, USA) was hydrolyzed to DCFH using NaOH (1 mM) for intracellular ROS detection. Rf (10 $\mu\text{g mL}^{-1}$), PEI-MnCO₃, and MRf NCs (100 $\mu\text{g mL}^{-1}$) was added to 2 mM H₂O₂, DCFH (1 μM) was added to the above solution and the mixture was exposure to LED light for 10 min, then their emission was monitored using a microplate reader (Ex/Em = 488/525 nm).

2.8 Biodegradation of MnCO₃ in TME simulation solution. PEI-MnCO₃ NCs were incubated in a solution of PBS (pH = 6.5) containing 2 mM H₂O₂ for 3, 12 and 24 h, respectively. The morphologic changes of the PEI-MnCO₃ NCs were observed using TEM. In addition, PEI-MnCO₃ NCs were incubated in PBS (pH = 6.5) for 10, 30, 60 and 120 min, the CO₂ contents was assessed by Meteorological chromatograph. After 2 h, the solution was centrifuged, the precipitates were analyzed using XPS.

2.9 $^1\text{O}_2$ Measurement. $^1\text{O}_2$ generation was measured using a 1,3-diphenylisobenzofuran (DPBF) probe. PEI-MnCO₃ NCs were incubated in a simulated TME solution (PBS (pH = 6.5) containing 2 mM H₂O₂). 2 μL of DPBF solution (10 mM, DMSO) was added to 200 μL of above solution. The absorbance of DPBF at 410 nm was recorded every 2 minutes by a microplate reader.

2.10 Cell lines. The mouse TNBC cell line 4T1 and L929 cells were obtained from American Type Culture Collection. 4T1-Luc cells were maintained in RPMI 1640 medium (Sigma) with 10% FBS and penicillin (100 U/mL) and streptomycin (100 $\mu\text{g}/\text{mL}$) (Invitrogen). L929 cells were maintained in Dulbecco's modified Eagle's medium (Sigma) with 10% fetal bovine serum (FBS, Gibco) and penicillin (100 U/mL) and streptomycin (100 $\mu\text{g}/\text{mL}$) (Invitrogen). The cells were cultured at 37 °C under a humidified atmosphere of 95% air and 5% CO₂ and the medium was changed every 2 days.

2.11 Cell viability. 4T1 and L929 cells were seeded in 96-well plates with a density of 5×10^4 cells per well, respectively. After culturing for 24 h, gradient concentrations of PEI-MnCO₃, Rf and MRf (500, 250, 125, 62.5, 31.25, 15.6, 7.8, 0 $\mu\text{g}/\text{mL}$) were co-cultured with the cells for another 24 h. Then, MTT assay was measured according to the standard protocol.

2.12 Transfection of pDNA. 4T1 cells were seeded in 6-well plates with a density of 5×10^4 cells per well. The medium was removed with fresh 1640 medium without FBS. All NCs were prepared by MRf/pDNA with a weight ratio of 15/1. Then 15 μL MnCO₃/pDNA mixture was added to the 6-well plate co-cultured for 6 h. The medium was changed with fresh 1640 containing 10% FBS and 1% PS

2.13 Live/Dead Staining. 4T1 cells were seeded on 24-well plates at a concentration of 5×10^4 cells/cm² under 37°C with 5 % CO₂ for 24 h. 200 μL of PEI-MnCO₃ ($50 \mu\text{g mL}^{-1}$), Rf ($50 \mu\text{g mL}^{-1}$), MRf ($50 \mu\text{g mL}^{-1}$), MRp ($50 \mu\text{g mL}^{-1}$) were added to the plate, then those groups were exposure to LED light or in dark for 10 min, respectively. After co-cultured for 24 h, the cells were subject to Live/Dead staining following the manufacturer's protocol (Sigma, USA) and imaged under a fluorescence microscope (DMI4000, Leica).

2.14 Intracellular ROS Detection. Intracellular ROS production was detected by DCFH-DA. In brief, 4T1 cells were seeded in 24-well plate (1×10^5 cells per mL) and cultured overnight. Then cells were treated similarly as above (as live/dead staining). Finally, the cells were incubated with DCFH-DA probe (1 μM) for 15 min, washed with PBS and observed by fluorescence microscopy. Moreover, their quantitative analysis was using a multifunctional microplate reader (Ex/Em: 488/525 nm).

2.15 Intracellular pH Detection. The changes of intracellular pH were using a intracellular pH fluorescence probe (BCECF AM). Briefly, the 4T1 cells were treated with PEI-MnCO₃ NCs ($50 \mu\text{g mL}^{-1}$) as experiment group and medium as control group, then the cells were cultured with BCECF AM (5 μM) for 20 min, and their images were observed under fluorescence microscopy. And their quantitative analysis was using a multifunctional microplate reader (Ex/Em: 488/535 nm).

2.16 Animals. Balb/c nude mice (six-week-old, female) were purchased from Guangdong Medical Lab. Animal Center. The protocol was approved by Institutional Animal Care and Use Committee of General Hospital of Southern Theater Command of PLA.

2.17 In vivo tumor therapy. 5×10^6 4T1 cells were injected to the second breast nodule of the nude mice. After the tumors grew to a size of 50 – 70 mm², the mice were divided into 5 random groups (n = 4) undergoing different treatments: 1) PBS; 2) PEI-MnCO₃; 3) Rf + LED light; 4) MR + Light; 5) MRp + LED light; The NCs were injected intratumorally into the 4T1-bearing mouse. The size of the tumors was measured every other day for two weeks. The tumor volumes were carefully measured every other day for 14 days by a caliper and calculated as **Equation S2**:

$$V = \frac{ab^2}{2}$$

2

where $V(\text{mm}^3)$ is the volume of the tumor, and a (mm) and b (mm) is length of tumor and width of tumor, respectively. Then the tumors were histologically analyzed by hematoxylin and eosin (H&E) staining.

3. Results And Discussion

3.1 Characterization of MRp NCs. Firstly, the monodisperse MnCO₃ NCs were prepared by a microemulsion method according to our previous method¹⁶. Transmission electron microscope (TEM) image (Fig. 1a) revealed that the MnCO₃ NCs had cubic-like morphology with particle size of ca. 120 nm. As shown in Fig. 1b, high resolution TEM image with a typical individual nanocube inset revealed its highly porous nature and the marked lattice spacings of 0.285 nm which could be indexed to the (104) planes of MnCO₃. X-ray diffraction (XRD) pattern was employed to detect the crystalline phase and purity of the samples. The results (Fig. 1c) revealed that the samples were pure rhombohedral MnCO₃ (JCPDS Card No. 44-1472). In addition, the porous structure of the MnCO₃ NCs was investigated by Brunauer–Emmett–Teller (BET) analysis. As depicted in Fig. 1d and e, the PEI-MnCO₃ NCs exhibited high Brunauer–Emmett–Teller surface area ($49.97 \text{ m}^2 \text{ g}^{-1}$) and pore volume ($0.293 \text{ cm}^3 \text{ g}^{-1}$), respectively. The average pore size is about 3.41 nm according to the N₂ adsorption–desorption isotherms. Zeta potential of the CTAB-MnCO₃, fine MnCO₃ (removal of CTAB) and PEI-MnCO₃ were shown in Fig. 1f, illustrating the successful modification of PEI. The porous structure of the PEI-MnCO₃ NCs endows them with excellent Rf loading capacity. As can be seen in Fig. 1g, the loading efficiency (w.t %) of Rf in PEI-MnCO₃ NCs was calculated as high as 90%, confirmed by the absorption spectra. More importantly, the PEI-MnCO₃/Rf (MRf) NCs presented high binding ability to pDNA because of their high zeta potential. The binding ability was investigated by gel retardation assays (as shown in Fig. 1h), the results illustrated that the iSur-pDNA could be completely loaded onto MRf NCs at the weight ratios of 1:15. Moreover, we have assessed the ROS production ability of PEI-MnCO₃. Rf and MRf under the same condition using 5, 5-dimethyl-1-

pyrroline-N-oxide (DMPO) as trapping agent. Inspiringly, MRf NCs exhibited significantly enhanced ROS production than PEI-MnCO₃ and Rf, respectively (Fig. 1i).

3.2 TME responsive characters. To verify the TME responsive characters of the PEI-MnCO₃ NCs, we systematically analyzed their degradation characters, catalytic ability, and gas production under simulated TME (pH = 6.5, 2 mM H₂O₂, 8 mM glutathione). As can be seen in Fig. 2a, PEI-MnCO₃ NCs worked as a H₂O₂ catalyst, which could catalyze H₂O₂ to produce O₂ (Fig. 2a). Meanwhile, they decomposed slowly and produced CO₂ (Fig.s S1 and S2). Their morphology changes were observed by TEM, illustrating a dynamic changes of morphology, i.e., cubic-round-circle-dots, and PEI-MnCO₃ NCs finally could be degraded into tiny round nanodots. Notably, the O₂ production soared to 18.1 μg mL⁻¹ while the CO₂ production was in a relatively low speed (Fig.s 2a, S2). During the catalytic process, PEI-MnCO₃ NCs degraded into small pieces (Fig.s S1), release Mn²⁺ and OH⁻ (Caption 1, 2), the OH⁻ ion is beneficial to improve the acidic TME while Mn²⁺ facilitate the fenton reaction¹⁷ (Caption 2, 3) in tumors. To prove this process, we carried out XRD to evaluate the NCs in simulated TME, the results indicated the partially degraded NCs were still MnCO₃ without any impurities (Fig.s S3). The multivalence Mn in XPS spectra further confirmed the release of OH⁻ and the redox reaction in this process (Fig.s S4). As expected, we discovered ¹O₂ generation in PEI-MnCO₃ NCs during degradation, which is beneficial for CDT (Fig. 2b and c, Eq. 2, 3). Considering that Rf-mediated PDT consumes O₂ in hypoxia TME, O₂ produced by PEI-MnCO₃ NCs may improve the efficacy of PDT (Eq. 4f, Fig. 2b). Subsequently, we investigated whether the MRf produced more ROS compared with single Rf group under simulated TME solution when illuminated by white-light LED light. Both MRf and Rf generated ROS (Fig. 2c). Notably, the MRf could enhance the ROS production during the observing time (10 min) and this phenomenon could be repeated 5 times, indicating that PEI-MnCO₃ NCs as drug loading carriers could significantly improve ROS production as well as protect Rf from photobleaching and photodamage¹⁸ (Fig. 2d).



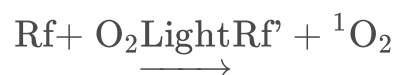
1



2



3



4

Note: Rf' is the excited Rf.

3.3 Cellular ROS production and pH responsive ability. Thanks to the excellent performance of MnCO_3 -based NCs in TME, we then investigated their cancer-killing efficiency. Firstly, the intracellular ROS production was monitored by using the green probe, 2',7'-dichlorofluorescein diacetate (DCFH-DA). As shown in Fig. 3a and d, the cells treated with MRf + LED light exhibited much stronger fluorescent intensity than Rf + LED light and PEI- MnCO_3 + LED light groups. By contrast, the groups (control group, PEI- MnCO_3 , Rf and MRf) without LED illumination showed weak fluorescence. The results suggested that the ROS production capability of Rf could be significantly improved by PEI- MnCO_3 *in vitro*. Next, we tested the changes of intracellular acidity because of the OH^- release and pH-sensitive characters of PEI- MnCO_3 NCs. Noteworthy, the synthesized MnCO_3 NCs exhibited better pH stability than commercial MnCO_3 (Fig. 3c), which may attribute to their high surface area and porous structure. The green pH probe (2',7'-bis(carboxyethyl)-5(6)-carboxyfluorescein, BCECF) was employed to investigate the intracellular pH changes of 4T1 cells after different treatments. As illustrated in Fig. 3b, the PEI- MnCO_3 treated cells exhibited much stronger fluorescence intensity than the control group, suggesting they could improve the acidic environment in tumor cells (Fig. 3b, e). Such an interesting pH improvement will help to destroy lysosomes and ameliorate TME ability, thus accelerating the death of cancer cells.

3.4 The killing effect of MRp NCs on TNBC cells in vitro. To verify the biocompatibility and anticancer effect of the synthesized NCs, MnCO_3 and PEI- MnCO_3 NCs with different concentrations were co-cultured with 4T1 cells and L929 cells, respectively. As shown in Fig. 4a and b, 4T1 cells were significantly destroyed by MnCO_3 and PEI- MnCO_3 NCs ($p < 0.05$) compared to L929 cells under the same condition, which illustrated the TME-responsive characters and selective toxicity of PEI- MnCO_3 NCs on cancer cells. Moreover, we investigated the cancer-killing effects of MnCO_3 -based NCs, i.e. PEI- MnCO_3 , Rf, MRf, and MRp in dark or under LED light. As expected, MRp + LED light exhibited the highest toxicity to 4T1 cells, suggesting CDT, PDT and pDNA comprised an enhanced tumor therapeutic efficacy. Furthermore, the live/dead staining was employed to investigate the cell status with different treatments. As compared to normal cells, 4T1 cells suffered from different levels of damage in the MnCO_3 -related groups. Specifically, all the cancer cells in MRf + light group became red (death) and round, the results further confirmed their excellent tumor-killing effect (Fig. 4).

3.5 Intracellular distribution and characters in 4T1 cells. Because of the high killing efficiency of MnCO_3 -based NCs, we next investigated the behaviors of NCs in 4T1 cells. As shown in Fig. 5a, the FITC- MnCO_3 NCs was distributed in the cytoplasm, some of them around the lysosomes, with an overlap coefficient of 50% with the lysosome at the first 6 h; With the increase of time, the FITC- MnCO_3 NCs fluorescence area covers 81% of lysosomes at 24 h, illustrating a lysosome targeted effect (Fig. 5a, g). The acidic environment in lysosome is beneficial to the degradation of MnCO_3 -based NCs, and the alkaline environment provided by MnCO_3 NCs will destroy lysosomes, thus accelerating the death of cancer cells.

Hypoxia is an important character of solid tumors, which contribute greatly to tumor metastasis and the resistance to radio/chemotherapy¹⁹. Moreover, hypoxia also limited the efficiency of PDT and CDT²⁰.

Hypoxia-inducible factor-1 α (HIF-1 α) is highly active under hypoxic conditions, resulting in the changes of caspase-3 and Bax expression in tumors²¹. Here, the relief of hypoxia in PEI-MnCO₃ was evaluated both by hypoxia probe and Western blot. As shown in Fig. 5b and c, the red fluorescence in hypoxia treatment group was significantly enhanced compared with the untreated group. In contrast, the hypoxia cells co-cultured with PEI-MnCO₃ NCs showed weak red fluorescence, illustrating the relief of hypoxia by intracellular O₂ generation of MnCO₃ NCs.

Survivin is overexpressed in TNBC membranes²², moreover, active Survivin induces the abnormal expression of several genes, including Bcl-2, Bax, and caspase-3²³. We evaluated the transfection properties of PEI-MnCO₃. As shown in Fig. 6d, the FLUC-pDNA combined PEI-MnCO₃ NCs exhibited stronger red fluorescence intensity than the free FLUC-pDNA group, confirming the effective transfection efficiency of PEI-MnCO₃ NCs. The results were in accordance with Fig. 1h. Meanwhile, we examined the related protein expressions after different treatments. The results showed MnCO₃-based NCs treatment significantly decreased the HIF- α expression, thus improved the hypoxia status of tumors. Moreover, MRp knockdown the survivin gene in 4T1 cells. Together with the downregulation of HIF- α and survivin genes, the related pro-apoptotic proteins, caspase-3 and Bax were upregulated. These genes work together to accelerate the progress of cell apoptosis and death²⁴.

3.6 Therapeutic effect *in vivo*. The above results clearly confirm the anticancer ability of the MRp *in vitro*, we further evaluated their anticancer efficacy in tumor-bearing 4T1 mice. In the 4T1 tumor model (Bab/c nude mice), mice received PBS, MRp, MRf, Rf, PEI-MnCO₃ under LED light in tumor sites when their tumor size reached to 50–70 mm². Importantly, there was no thermal damage or surrounding tissue damage during the treatment process. After the treatment, the tumor size, body weight changes, and their activeness were observed every 2 days. As shown in Fig. 6a, b, the tumor volume was significantly inhibited in MRp, MRf and PEI-MnCO₃ groups during the observed period. However, the tumor in Rf + light treatment group exhibited first restrained effect and subsequently promoted dynamic changes. This is probably because that the ROS released by Rf + LED light inhibited the tumor growth at first, then the hypoxia caused by PDT promoted tumor growth. While MnCO₃-based groups exhibited better therapeutic effects than the control group because of the sustained TME improvement (pH, hypoxia) and ¹O₂ generation. In addition, there were no notable differences in body changes among all treatment groups, and the mice in PEI-MnCO₃ based treatment groups were active, indicating their potential biosafety. Furthermore, the hematoxylin and eosin (H&E) staining of the tumors illustrated the high complex and rich vessels in control tumor, suggesting the vigorous proliferation ability of TNBC tumors. In contrast, the tumor tissues in MRp + Light group suffered from great damage compared to other groups. Noteworthy, there were lots of bubbles-like destruction in tumor sites after treated with MnCO₃ based nanomaterials, suggesting the sustained CO₂ and O₂ generation could result in serious tumor destruction.

H&E staining of main organs (heart, liver, spleen, lung, and kidney) was performed after different treatments. As shown in Fig. 7, the myocardial cells and the glomeruli were intact and clear in the

treatment groups. The glomerulus the hepatocytes and splenocytes were normal, and no damage or inflammatory was observed in the examined organs relative to the control group.

4 Conclusions

In summary, the mesoporous PEI-MnCO₃ NCs serve as drug loading (Rf) and transfection system (pDNA) for efficient TNBC therapy have been established because of their porous structure and positive zeta potential. Importantly, the PEI-MnCO₃ NCs possessed TME-responsive characters, O₂ generation ability and Mn²⁺ mediated CDT. Significantly, the ROS production ability could be amplified and the suvivin gene was silenced by MRp, which efficiently inhibit TNBC growth both *in vitro* and *in vivo*. Interestingly, the bubble (O₂ and CO₂) produced in the therapeutic process also destroy the tumor tissue severely, which may provide a new idea for tumor therapy.

Declarations

Authors' contributions

Li, L. Huang and X. Yang synthesized all the compounds and nanoparticles mentioned and characterized them in this article. L. Chen, L. Li, X. Ye and Z. Lin conducted all cell experiments and animal experiments. L. Li wrote the manuscript with the help of all authors. X. Wei, X. Yang, and Z. Yang designed the experiments, and revised the manuscript. All authors read and approved the final manuscript.

Acknowledgements

This paper is dedicated to the memory of my respected tutor and friend, Prof. Mingying Peng. This work is financially supported by National Natural Science Foundation of China (52002133 and 51772336), Foundation for Basic and Applied Basic research of Guangdong Province (2019A1515110328), China Postdoctoral Science Foundation (2020T130210). Natural Science Foundation of Guangdong Province (2020A1515010398) and State Key Lab of Luminescent Materials and Devices.

Ethics approval and consent to participate

All animal experiments were carried out under the guidelines evaluated and approved by the ethics committee of General Hospital of Southern Theater Command of PLA (Resolution No. 2020-1108-2).

Consent for publication

All authors of this study agreed to publish.

Competing interests

The authors declare no competing financial interests

Availability of data and materials

All data generated or analyzed during this study are included in this published article and the Additional Information.

References

1. Cleator, S., Heller, W., Coombes, R. C., Triple-negative breast cancer: therapeutic options. *Lancet Oncol.* **2007**, *8*, 235-244.
2. Cardoso, F., Spence, D., Mertz, S., Corneliussen-James, D., Mayer, M., Global analysis of advanced/metastatic breast cancer: Decade report (2005-2015). *Breast* **2018**, *39*, 131-138.
3. Engebraaten, O., Vollan, H. K. M., Børresen-Dale, A.-L., Triple-Negative Breast Cancer and the Need for New Therapeutic Targets. *Am. J. Pathol.* *183* (4), 1064-1074.
4. Moloney, J. N., Cotter, T. G., ROS signalling in the biology of cancer. *Semin. Cell Dev. Biol.* **2017**, *80*, 50-64.
5. Liyanage, U. K., Moore, T. T., Joo, H. G., Tanaka, Y., Herrmann, V., Doherty, G., Drebin, J. A., Strasberg, S. M., Eberlein, T. J., Goedegebuure, P. S., Blood and Tumor Microenvironment of Patients with Pancreas or Breast Adenocarcinoma 1. *J. Immunol.* **2013**, *169* (5), 2756-61.
6. Li, L., Lu, Y., Jiang, C., Zhu, Y., Yang, X., Hu, X., Lin, Z., Zhang, Y., Peng, M., Xia, H., Mao, C., Actively Targeted Deep Tissue Imaging and Photothermal-Chemo Therapy of Breast Cancer by Antibody-Functionalized Drug-Loaded X-Ray-Responsive Bismuth Sulfide@Mesoporous Silica Core-Shell Nanoparticles. *Adv. Funct. Mater.* **2018**, *28* (5), 170462.
7. Li, L., Lu, Y., Lin, Z., Mao, A. S., Jiao, J., Zhu, Y., Jiang, C., Yang, Z., Peng, M., Mao, C., Ultralong tumor retention of theranostic nanoparticles with short peptide-enabled active tumor homing. *Mater. Horiz.* **2019**, *6* (9), 1845-1853.
8. Lu, Y., Li, L., Lin, Z., Li, M., Hu, X., Zhang Y., Peng M., Xia, H., Enhancing Osteosarcoma Killing and CT Imaging Using Ultrahigh Drug Loading and NIR-Responsive Bismuth Sulfide@Mesoporous Silica Nanoparticles. *Adv. Healthc. Mater.* **2018**, *7*, 1800602.
9. He, D., He, X., Wang, K., Yang, X., Yang, X., Zou, Z., Li, X., Redox-responsive degradable honeycomb manganese oxide nanostructures as effective nanocarriers for intracellular glutathione-triggered drug release. *Chem. Commun.* **2015**, *51* (4), 776-779.
10. Xu, X., Zhang, R., Yang, X., Lu, Y., Yang, Z., Peng, M., Ma, Z., Jiao, J., Li, L., A Honeycomb-Like Bismuth/Manganese Oxide Nanoparticle with Mutual Reinforcement of Internal and External Response for Triple-Negative Breast Cancer Targeted Therapy. *Adv. Healthc. Mater.* **2021**, doi.org/10.1002/adhm.202100518.
11. Li, L., Lu, Y., Xu, X., Yang, X., Chen, L., Jiang, C., Wang, Y., Hu, W., Wei, X., Yang, Z., Catalytic-Enhanced Lactoferrin-Functionalized Au-Bi₂Se₃ Nanodots for Parkinson's Disease Therapy via Reactive Oxygen Attenuation and Mitochondrial Protection. *Adv. Healthc. Mater.* **2021**, *10*, 2100316.

12. Lu, C., Zhang, C., Wang, P., Zhao, Y., Yang, Y., Wang, Y., Yuan, H., Qu, S., Zhang, X., Song, G., Pu, K., Light-free Generation of Singlet Oxygen through Manganese-Thiophene Nanosystems for pH-Responsive Chemiluminescence Imaging and Tumor Therapy. *Chem* **2020**, *6* (9), 2314-2334.
13. Lin, X., Liu, S., Zhang, X., Zhu, R., Chen, S., Chen, X., Song, J., Yang, H., An Ultrasound Activated Vesicle of Janus Au-MnO Nanoparticles for Promoted Tumor Penetration and Sono-Chemodynamic Therapy of Orthotopic Liver Cancer. *Angewan. Chem. Int. Edit.* **2020**, *59* (4), 1682-1688.
14. Ding, B., Zheng, P., Jiang, F., Zhao, Y., Wang, M., Chang, M., Ma, P. a., Lin, J., MnOx Nanospikes as Nanoadjuvants and Immunogenic Cell Death Drugs with Enhanced Antitumor Immunity and Antimetastatic Effect. *Angewan. Chem. Int. Edit.* **2020**, *132* (38), 16523-16526.
15. Yang, X. F., Yang, J. H., Zaghbi, K., Trudeau, M. L., Ying, J. Y., Synthesis of phase-pure Li₂MnSiO₄@C porous nanoboxes for high-capacity Li-ion battery cathodes. *Nano Energy* **2015**, *12*, 305-313.
16. Liu, C., Wang, D., Zhang, S., Cheng, Y., Yang, F., Xing, Y., Xu, T., Dong, H., Zhang, X., Biodegradable Biomimic Copper/Manganese Silicate Nanospheres for Chemodynamic/Photodynamic Synergistic Therapy with Simultaneous Glutathione Depletion and Hypoxia Relief. *ACS Nano* **2019**, *13* (4), 4267-4277.
17. Smith, E. C., Metzler, D. E., The Photochemical Degradation of Riboflavin. *J. Am. Chem. Soc.* **1963**, *85* (20), 3285-3288.
18. Prasad, P., Gordijo, C. R., Abbasi, A. Z., Maeda, A., Ip, A., Rauth, A. M., Dacosta, R. S., Wu, X. Y., Multifunctional Albumin-MnO₂ Nanoparticles Modulate Solid Tumor Microenvironment by Attenuating Hypoxia, Acidosis, Vascular Endothelial Growth Factor and Enhance Radiation Response. *ACS Nano* **2014**, *8* (4), 3202-3212.
19. Zhang, C., Qin, W.-J., Bai, X.-F., Zhang, X.-Z., Nanomaterials to relieve tumor hypoxia for enhanced photodynamic therapy. *Nano Today* **2020**, *35*, 100960.
20. Zhou, X., You, M., Wang, F., Wang, Z., Gao, X., Jing, C., Liu, J., Guo, M., Li, J., Luo, A., Liu, H., Liu, Z., Chen, C., Multifunctional Graphdiyne–Cerium Oxide Nanozymes Facilitate MicroRNA Delivery and Attenuate Tumor Hypoxia for Highly Efficient Radiotherapy of Esophageal Cancer. *Adv. Mater.* **2021**, *33*, 2100556.
21. Badana, A. K., Chintala, M., Gavara, M. M., Naik, S., Kumari, S., Kappala, V. R., Iska, B. R., Malla, R. R., Lipid rafts disruption induces apoptosis by attenuating expression of LRP6 and survivin in triple negative breast cancer. *Biomed. Pharmacother.* **2018**, *97*, 359-368.
22. Yan-Bo, Liu, Ling, Zhang, Ya-Xiong, Guo, Li-Fang, Gao, Xi-Chun, Liu, Plasmid-based Survivin shRNA and GRIM-19 carried by attenuated Salmonella suppresses tumor cell growth. *Asian J. Androl.* **2012**, *14* (4), 536-545.
23. He, Z., Ma, W.-Y., Hashimoto, T., Bode, A. M., Yang, C. S., Dong, Z., Induction of Apoptosis by Caffeine Is Mediated by the p53, Bax, and Caspase 3 Pathways. *Cancer Res.* **2003**, *63* (15), 4396-4401.
24. Antonio, C., Lin, K. Y., Cheng, S. M., Shing-Ling, T., Ju-Ya, T., Lin, C. H., Delivery of a survivin promoter-driven antisense survivin-expressing plasmid DNA as a cancer therapeutic: a proof-of-concept study. *Oncotargets Ther.* **2016**, *9*, 2601-2613.

Figures

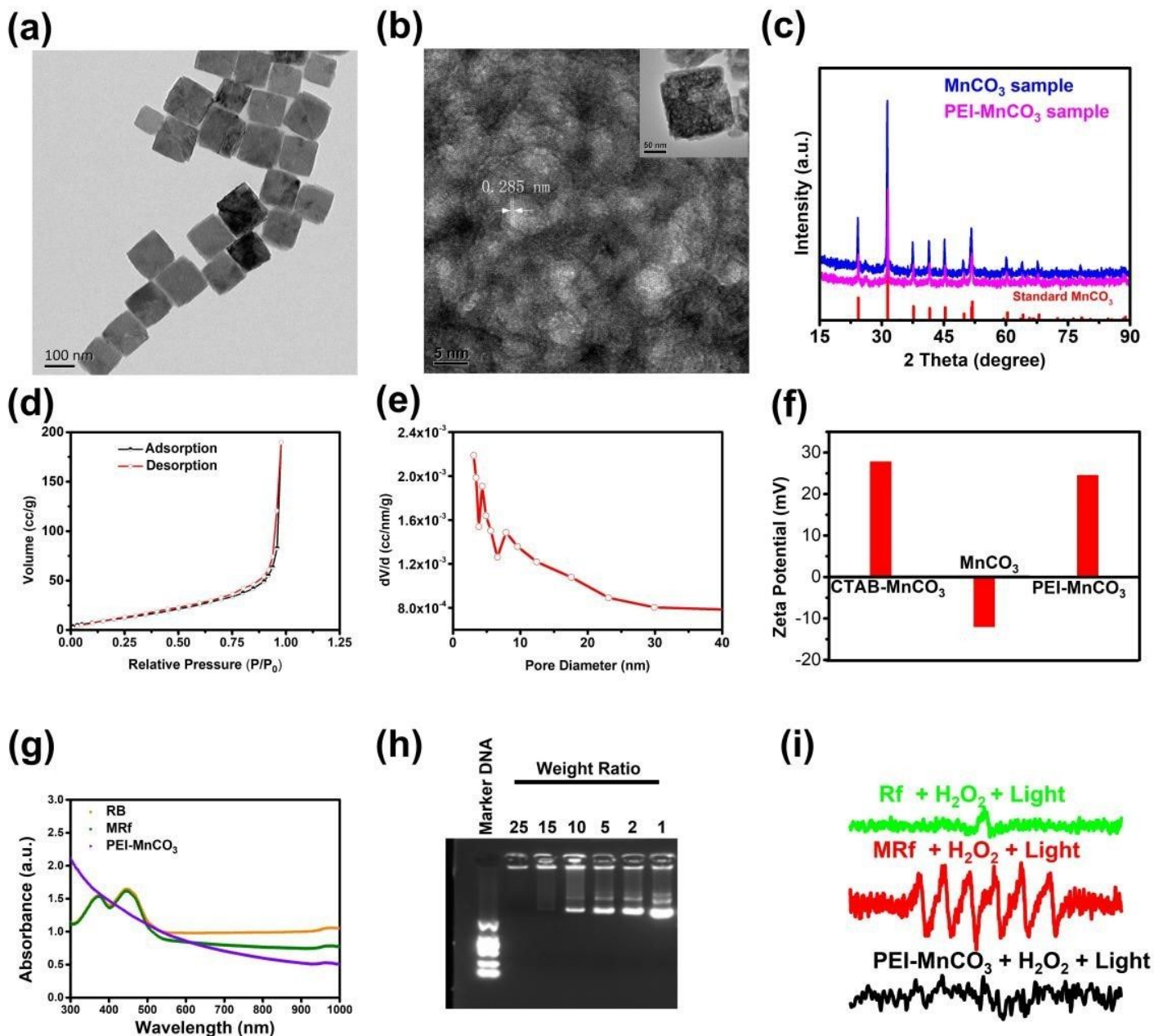


Figure 1

Characterization of MRp NCs. (a) Low magnification and (b) high resolution TEM images of MnCO₃ NCs. Inset, TEM of the corresponding MnCO₃ NC. (c) XRD spectra of MnCO₃ NCs and PEI-MnCO₃ NCs. (d) N₂ adsorption–desorption isotherms and (e) desorption pore size distribution of PEI-MnCO₃ NCs. (f) Zeta potential of CTAB-MnCO₃, fine MnCO₃ (washed out CTAB) and PEI-MnCO₃. (g) Absorbance spectra of PEI-MnCO₃, Rf and MRf. (h) Agarose-gel electrophoresis of MRf and pDNA at different weight ratios. (i) Electron spin trapping (ESR) spectra of PEI-MnCO₃, Rf and MRf with H₂O₂ (10 mM) under LED light using DMPO.

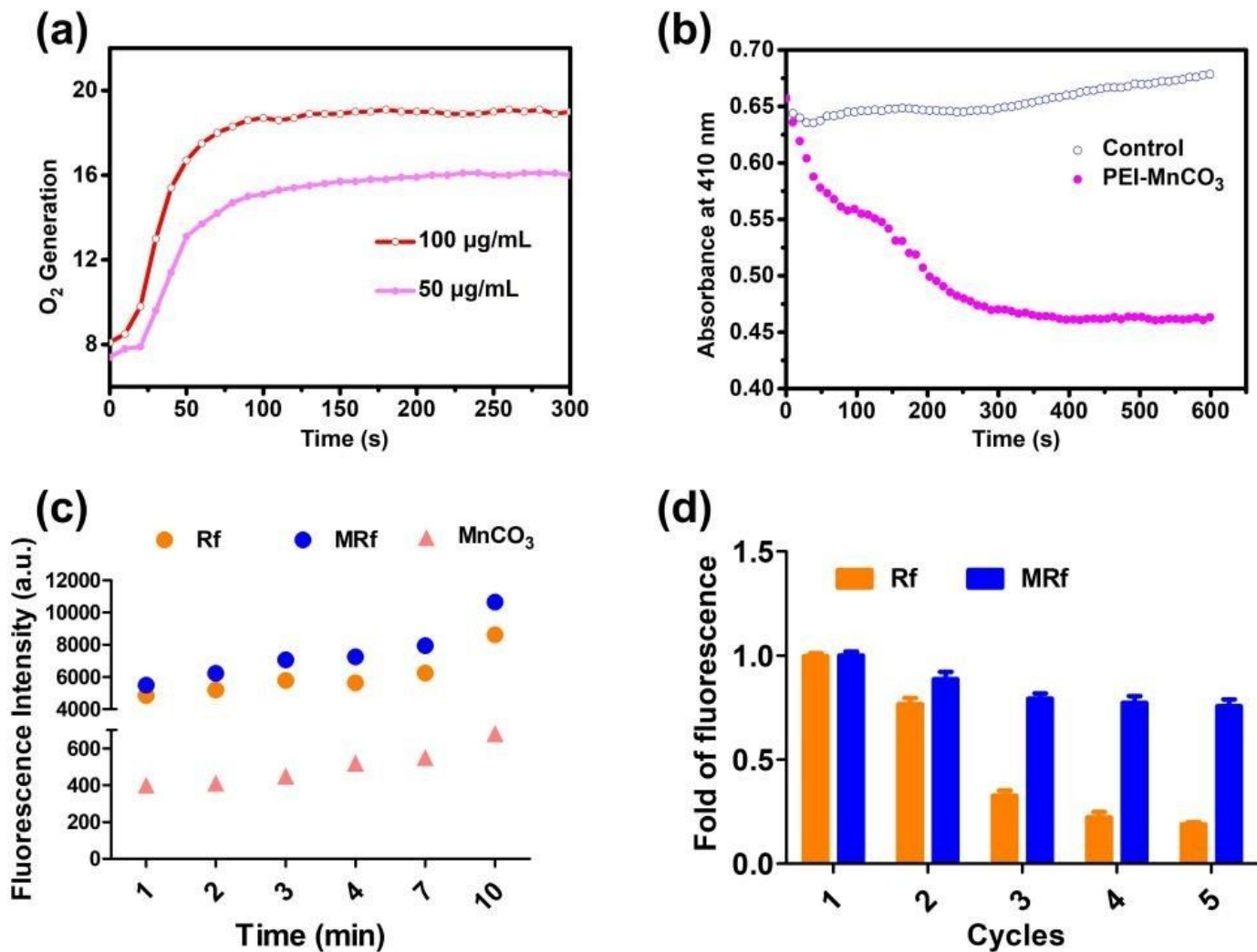


Figure 2

Enhanced CDT effect of MRf NCs. (a) O₂ generation ability of PEI-MnCO₃ NCs. (b) Dynamic changes of DPBF with PEI-MnCO₃ NCs. (c) Time-dependent generation of ROS under LED light. (d) Stability of Rf and MRf under 5 cycles of LED light irradiation, data are represented as mean ± standard deviation (SD). All the above experiments were conducted in simulated TME (2 mM H₂O₂, pH=6.5, 2 mM GSH) solution.

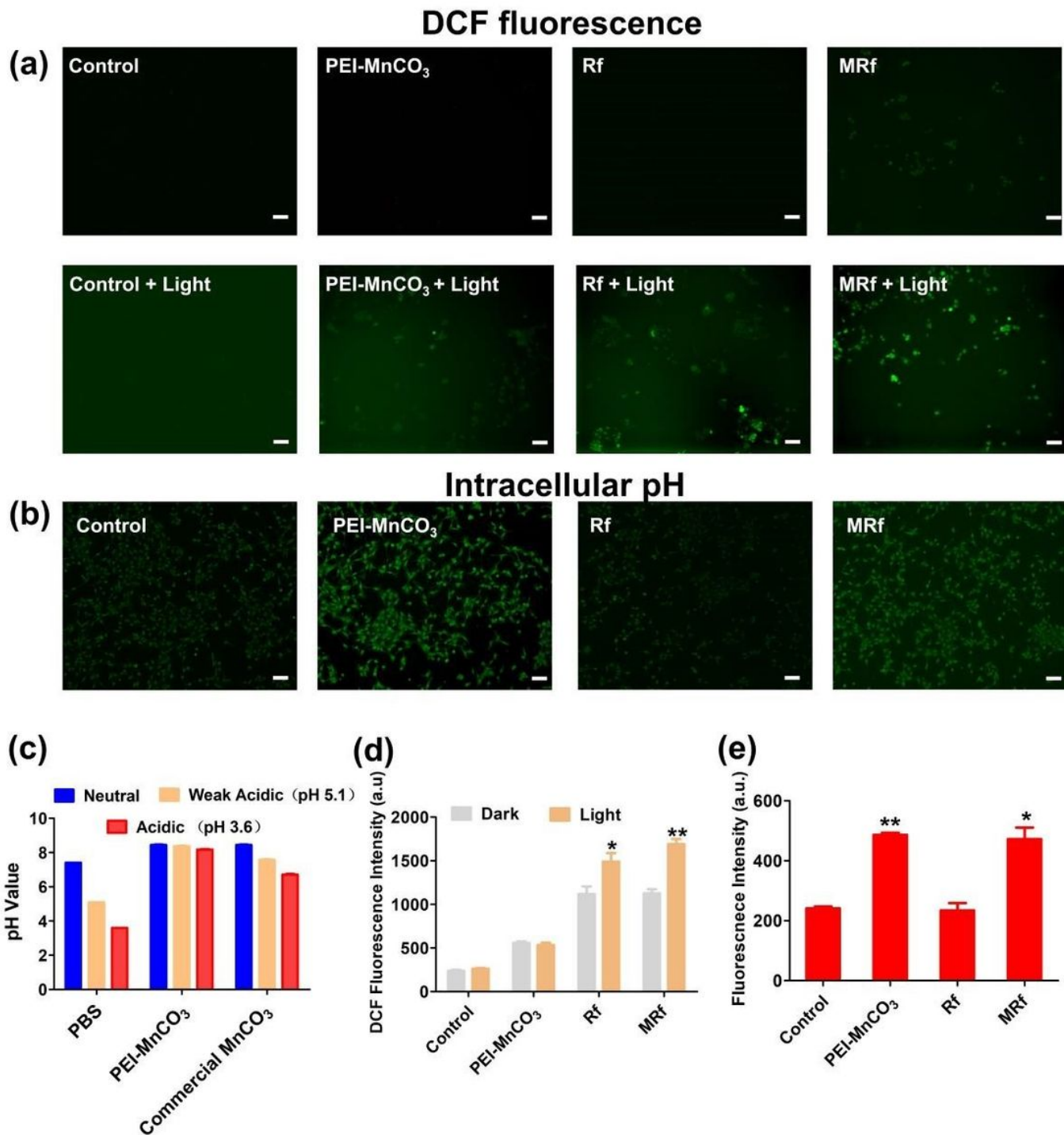


Figure 3

Tumor microenvironment responsive ability of MRf NCs. (a) DCF fluorescence (ROS level) images of 4T1 cells after different treatment. (b) BCECF fluorescence (pH changes) images of 4T1 cells after different treatment. (c) pH changes of different pH PBS solutions after PEI-MnCO₃ and commercial MnCO₃ treatment. (d) DCF fluorescence intensity in different treatment groups (Ex/Em=488 nm/525 nm). (e) BCECF fluorescence intensity in different treatment groups (Ex/Em=430 nm/530 nm). Data are represented as mean ± SD; n=4; Statistical significance was analyzed by the two-tailed Student's t-test.

*p<0.05, **p<0.01. All light treated groups were compared to the dark treated group in c. And all groups are compared to control group in d.

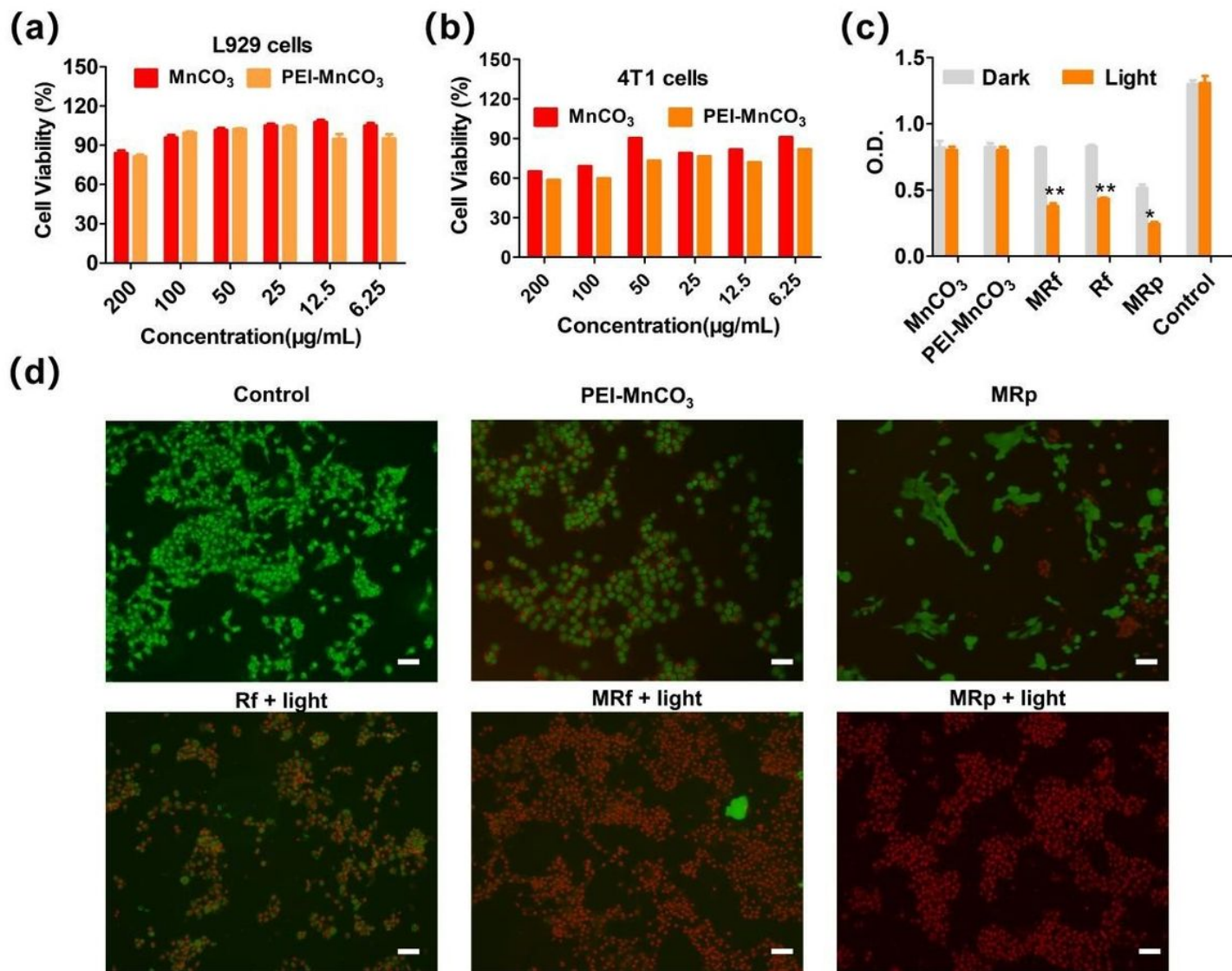


Figure 4

Cell viability. (a) Cell viability of L929 cells after treated with MnCO₃ and PEI-MnCO₃ NCs. (b) Cell viability of 4T1 cells after treated with MnCO₃ and PEI-MnCO₃ NCs. (c) Cell killing effect of different treatment on 4T1 cells in dark or under LED light. Data are represented as mean ± standard deviation (SD); n=4; Statistical significance was analyzed by the two-tailed Student's t-test. *p<0.05, **p<0.01. All light treated groups were compared to the dark treated group. (d) Live/dead staining of 4T1 cells with different treatment, scale bar=50 µm.

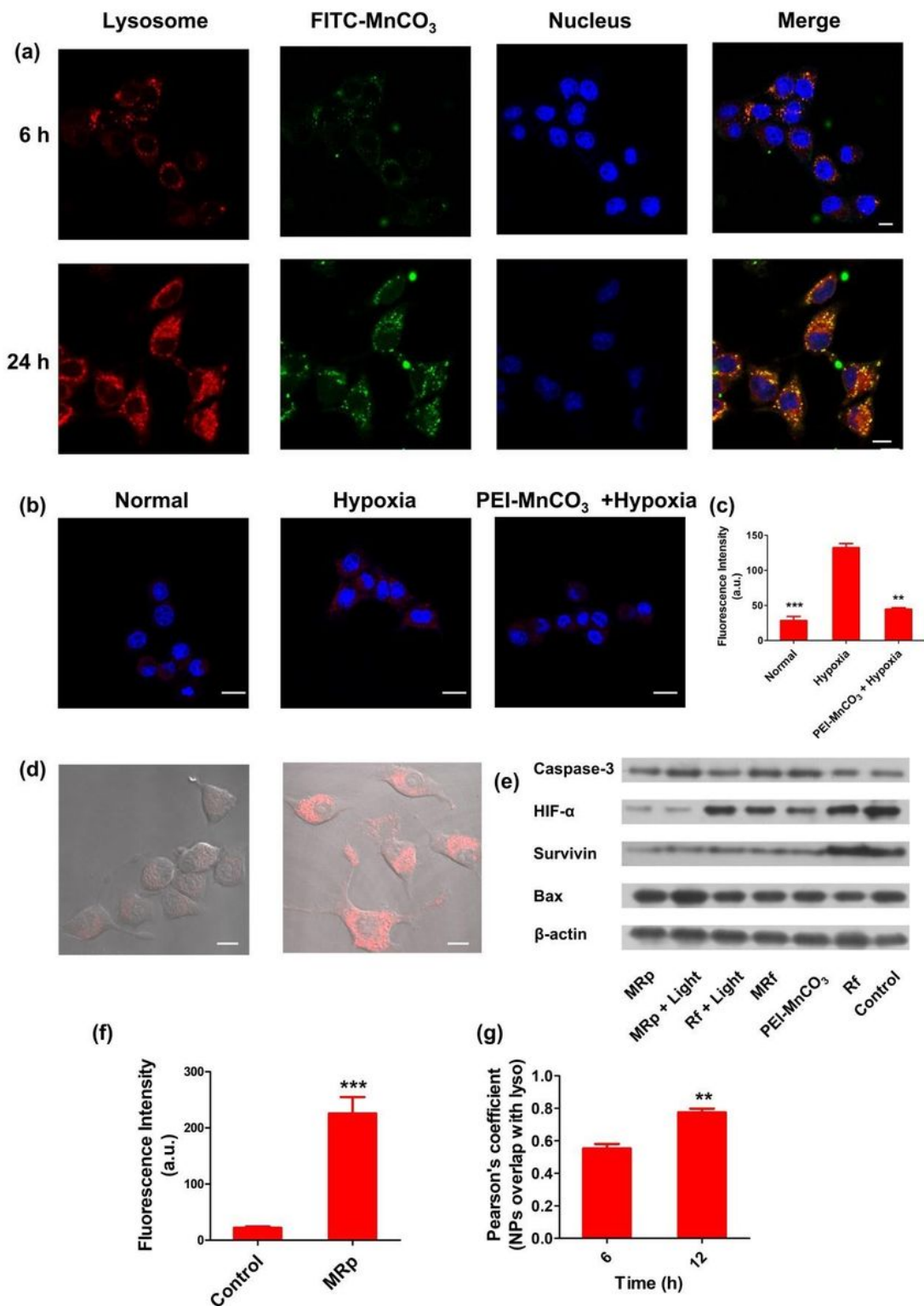


Figure 5

Behaviors of MnCO₃ in 4T1 cells. (a) Distribution of FITC-MnCO₃ NCs in 4T1 cells, lysosome (red), MnCO₃ (green), Hoechst 33342 (blue), the scale bar in the above Fig.s is 10 μm. (b) Fluorescence images of 4T1 cells treated with PEI-MnCO₃ NCs for relief of hypoxia. (c) Fluorescence intensity of hypoxia-probe (Ex/Em=488 nm/580 nm) in different groups. (d) Fluorescence images of 4T1 cells after transfected with MRp (the p-DNA was labeled with firefly luciferase (FLUC)). Left: control cells; right: MRp transfected

cells. (e) Changes in the expression of target proteins after different treatments. (f) Fluorescence intensity of FLUC probe in 4T1 cells ($E_m=540$ nm). (g) Pearson's coefficient of PEI-MnCO₃ NCs overlap lysosome (From Fig. 6a). Data are represented as mean \pm SD; n=4; Statistical significance was analyzed by the two-tailed Student's t-test. * $p<0.05$, ** $p<0.01$.

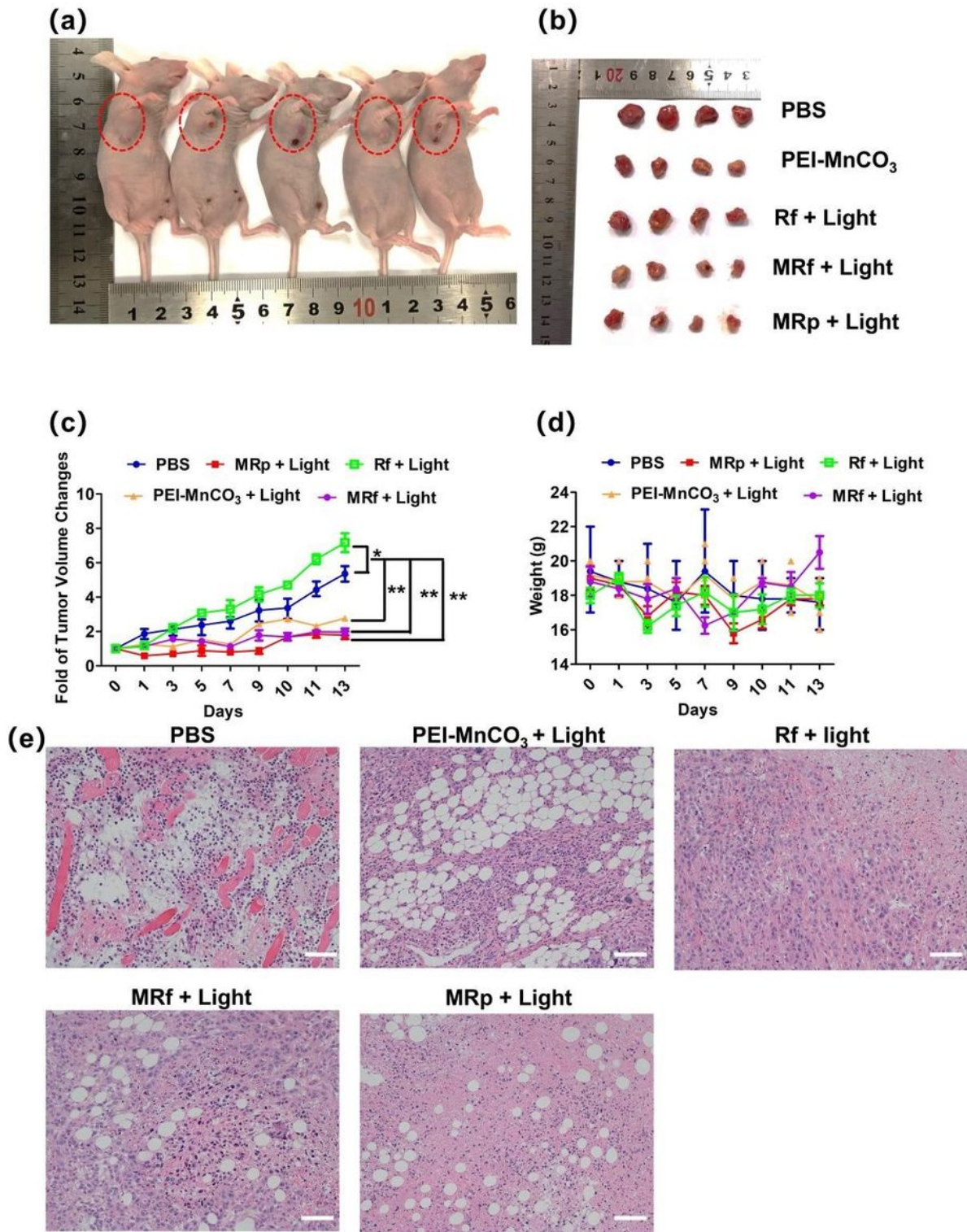


Figure 6

Therapeutic effect of different groups in vivo. (a) Representative images of 4T1-bearing nude mice in different groups at day 14. (b) Tumors collected from different groups of mice at day 14. (c) Tumor growth curves and (d) body weight changes of mice after different treatment during 14 days. (e) H&E staining of tumor sites after different treatment. Scale bar=50 μ m.

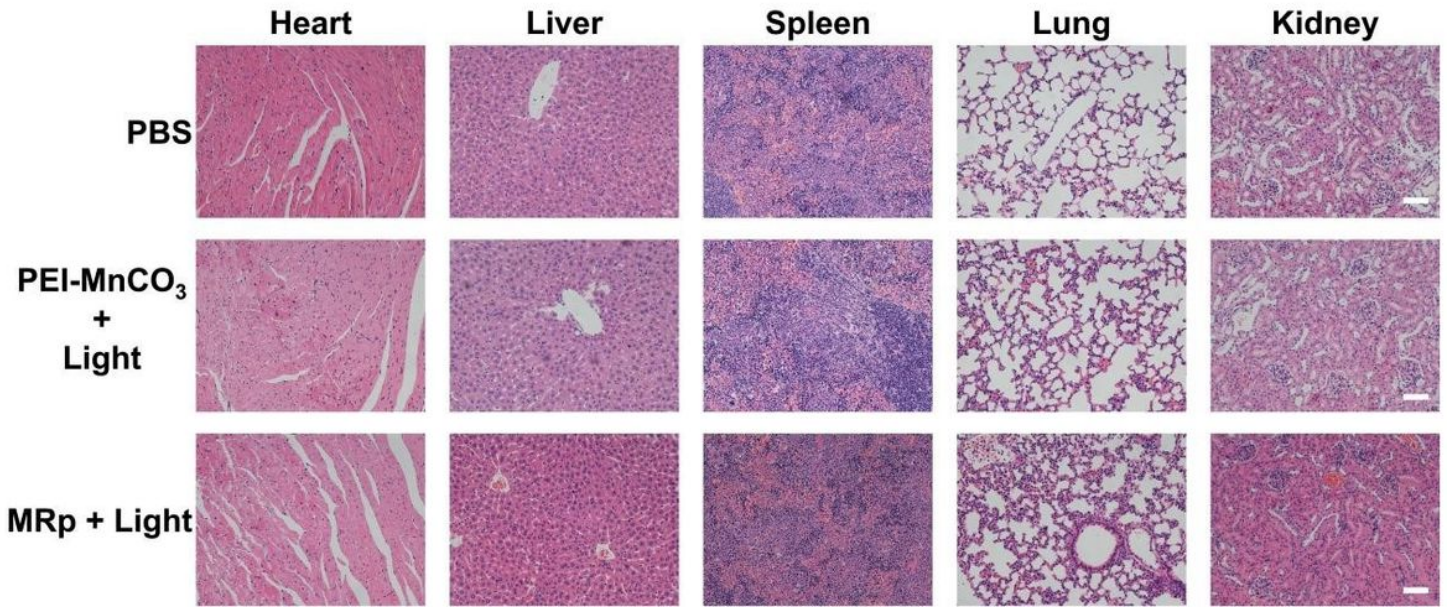


Figure 7

H&E staining of the main organs in PBS, PEI-MnCO₃ + Light, and MRp + Light group. Scale bar=50 μ m.

Supplementary Files

This is a list of supplementary files associated with this preprint. Click to download.

- [supportinginforMnCO3v6.docx](#)
- [Scheme1.jpg](#)